Numerical simulation of finite Reynolds number suspension drops settling under gravity

Thorsten Bosse, Leonhard Kleiser, and Carlos Härtel[a)]
Institute of Fluid Dynamics, ETH Zürich, Zürich, Switzerland

Eckart Meiburg
Department of Mechanical and Environmental Engineering, University of California at Santa Barbara, Santa Barbara, California 93106

(Received 6 August 2004; accepted 30 November 2004; published online 2 February 2005)

A suspension drop is a swarm of particles that are suspended in initially still fluid. When settling under the influence of gravity a suspension drop may undergo a complex shape evolution including the formation of a torus and eventual disintegration. In the present work the settling process of initially spherical suspension drops is investigated numerically for low and moderate drop Reynolds numbers Re_d. In the simulations a pseudospectral method is used for the liquid phase combined with a Lagrangian point-particle model for the particulate phase. In the case of low Reynolds numbers ($\mathrm{Re}_d < 1$) the suspension drop retains a roughly spherical shape while settling. A few particles leak away into a tail emanating from the rear of the drop. Due to the use of periodic boundaries a hindered settling effect is observed: the drop settling velocity is decreased compared to a suspension drop in infinite fluid. In the Reynolds number range $1 \leqslant \mathrm{Re}_d \leqslant 100$ the suspension drop deforms into a torus that eventually becomes unstable and breaks up into a number of secondary blobs. This Reynolds number range has not been investigated systematically in previous studies and is the focus of the present work. It is shown that the number of secondary blobs is primarily determined by the Reynolds number and the particle distribution inside the initial drop. An increased number of particles making up the suspension, i.e., a finer drop discretization, may result in a delayed torus disintegration with a larger number of secondary blobs. The influence of the initial particle distribution as a source of (natural) perturbations and the effect of initially imposed (artificial) shape perturbations on the breakup process are examined in detail. To gain a better understanding of the substructural effects (inside the suspension) leading to torus breakup, the particle field is analyzed from a spectral point of view. To this end, the time evolution of the Fourier coefficients associated with the particle distribution in the azimuthal direction of the torus is studied. © *2005 American Institute of Physics*. [DOI: 10.1063/1.1851428]

I. INTRODUCTION

Particle suspensions are a special class of multiphase flow systems that are frequently encountered in nature as well as in engineering applications. Natural occurrences range from large-scale phenomena such as particle sedimentation in river beds or dust particle transport in the atmosphere, to small-scale phenomena such as atherosclerotic deposits in human blood vessels. Engineering applications are numerous in the chemical and pharmaceutical industries including mixing, drying, and transport processes. Due to this wide variety of applications a considerable effort has been directed to developing numerical methods for the simulation of particle-laden flows. Examples include the trajectory and the two-fluid approach (Crowe *et al.*[1]), Stokesian dynamics simulations (Brady and Bossis[2]), lattice Boltzmann methods (Chen and Doolen[3]), statistical approaches using particle probability density functions (Reeks[4]), as well as direct numerical simulations (Pan *et al.*,[5] Glowinski,[6] Glowinski *et al.*[7]). However, many phenomena observed in particulate two-phase flows are still poorly understood including fundamental aspects of particle-fluid interaction.

A simple yet fundamental example of particle sedimentation is the behavior of a suspension drop settling in a fluid under the influence of gravity. A suspension drop is an initially spherical swarm of small particles that are suspended in initially quiescent fluid (the term "drop" is used as a synonym for "suspension drop" throughout this paper). Only recently the phenomena observed when a suspension drop settles under gravity have gained an increased interest. Nitsche and Batchelor[8] numerically investigated spherical suspension drops falling under creeping flow conditions. In this case the drop essentially retains its spherical shape while a few particles leak from the drop into a tail. Nitsche and Batchelor focused on the substructural effects of hydrodynamic diffusion and dispersion. In their paper they give a theoretical argument for the drop settling velocity and provide a semiempirical correlation for the rate of particle leakage from the blob. Machu *et al.*[9] did computer simulations and experiments of single suspension drops and pairs of trailing drops. They point out the crucial role of the initial drop shape. Under Stokes flow conditions an initially pearlike

[a)]Present address: General Electric Global Research—Europe, Munich, Germany.

shape, for example, causes the suspension drop to deform into a torus that eventually becomes unstable and breaks up into secondary blobs. These blobs deform into tori themselves resulting in a cascade process of blob deformations and breakups. This behavior of suspension drops is analogous to that of liquid drops settling in a fluid of smaller density. As opposed to suspension drops, a considerable amount of research work has been devoted to single and trailing liquid drops and fluid rings including theoretical studies (e.g., Kojima *et al.*[10]), numerical investigations (e.g., Koh and Leal,[11] Pozrikidis[12]), and experiments (e.g., Baumann *et al.*[13]). For a comprehensive review of previous work in this field the reader is referred to Machu *et al.* Walther and Koumoutsakos[14] performed simulations of falling suspension drops using a particle vortex method. Their results served primarily for validation purposes of their numerical method.

Nitsche and Batchelor[8] as well as Machu *et al.*[9] used Stokeslets in their simulations to represent the particles. The flow field was assembled as a superposition of Stokes flow disturbances caused by the particles. This approach is limited to the Stokes flow regime with vanishing drop Reynolds numbers ($\mathrm{Re}_d \ll 1$). The primary objective of our research work presented in this paper is to systematically investigate the settling behavior of suspension drops in a range of moderate Reynolds numbers ($1 \leqslant \mathrm{Re}_d \leqslant 100$). We aim at clarifying the Reynolds number dependence of the instability leading to torus breakup. Moreover, we examine in detail the role of the (initial) particle distribution and the number of particles inside the drop, as well as the effect of initial shape perturbations. These issues have not been addressed in previous studies.

The paper is organized as follows. In Sec. II, the governing equations are presented, along with the dimensionless parameters and the basic features regarding the numerical simulation approach. In Sec. III validation results for the case of Reynolds numbers much smaller than unity are given. In Sec. IV, we will at first focus on unraveling the physics of suspension drops for Reynolds numbers up to the order of 100, which represents the primary goal of the present investigation. However, in the course of this analysis, a number of questions arise that are intimately linked to the features of the numerical simulation technique. Therefore, these numerical issues will be addressed in a brief manner as well. Towards the end of Sec. IV the results of a spectral analysis of the settling drop and torus are presented, which provide additional insight into the time evolution of the particle field. Section V summarizes our findings and provides the main conclusions of the investigation.

II. SIMULATION APPROACH

The numerical method employed to solve the governing equations is known as the Eulerian–Lagrangian approach for particulate flows. The fluid equations are solved in an Eulerian framework using a Fourier pseudospectral method, whereas the particles are individually tracked along their trajectories.

A. Governing equations

We consider a dilute particle suspension, in which the particle concentration is small enough for interparticle collisions to be neglected. Moreover, the particles are assumed to be much smaller than the smallest relevant scales of the fluid motion. This allows for the particles to be modeled as point forces without resolving their finite size. The trajectory of a single particle is given by

$$\frac{dY_i(t)}{dt} = v_i(t), \tag{1}$$

where $Y_i(t)$ is the particle position, $v_i(t)$ the particle velocity, $Y_i(0) = Y_i^{(0)}$ its initial position, and $i = 1,2,3$ denotes the three spatial directions. The particle motion is governed by the equation derived by Maxey and Riley[15] in 1983, simplified for small heavy particles,

$$m_p \frac{dv_i(t)}{dt} = 6\pi\mu r(u_i[\vec{Y}(t),t] - v_i(t)) + (m_p - m_f)g_i \tag{2}$$

with m_p being the particle mass, m_f the mass of the fluid displaced by a particle, μ the dynamic viscosity, r the particle radius, $u_i[\vec{Y}(t),t]$ the fluid velocity at the instantaneous particle position, and g_i the gravitational acceleration. The first and second term on the right-hand side correspond to Stokes drag and net gravitational force, respectively. Assuming very small particles and relatively long fluid time scales, Eq. (2) can further be simplified by neglecting particle inertia (Maxey *et al.*[16]). In this case the particle motion is governed by a quasisteady equilibrium between drag forces on the particle's surface and forces due to gravity,

$$v_i(t) = u_i(\vec{Y}(t),t) + \tau_p g_i\left(1 - \frac{\varrho}{\varrho_p}\right). \tag{3}$$

Here $\tau_p = m_p/(6\pi\mu r)$ denotes the particle response time, ϱ the fluid density, and ϱ_p the particle density.

The fluid motion is governed by the continuity equation,

$$\frac{\partial u_i}{\partial x_i} = 0, \tag{4}$$

and the incompressible Navier–Stokes equation augmented by a source term representing the particles' feedback force,

$$\frac{\partial u_i}{\partial t} + u_m \frac{\partial u_i}{\partial x_m} = -\frac{1}{\varrho}\frac{\partial p}{\partial x_i} + \nu \frac{\partial^2 u_i}{\partial x_m \partial x_m} + \frac{1}{\varrho} f_i^{(p)}, \tag{5}$$

with the two-way coupling term

$$f_i^{(p)} = -\frac{6\pi\mu r \varrho_p}{m_p} \sum_{j=1}^{n_p^r} (u_{i,j}(\vec{Y}_j) - v_{i,j})\,\delta(x_i - Y_{i,j}). \tag{6}$$

Here, $\nu = \mu/\varrho$ is the kinematic viscosity, n_p^r is the number of (real) particles. The Dirac δ function indicates that the feedback force of particle j is applied as a point force at the instantaneous particle position $Y_{i,j}(t)$.

B. Dimensionless parameters

There is a total of seven independent physical quantities that uniquely describe the properties of a suspension drop settling in a fluid under gravity. The fluid is characterized by its density ϱ and its dynamic viscosity μ. A single spherical particle is characterized by two quantities, e.g., the particle mass m_p and the particle radius r. Alternatively, one or both of these two could be replaced by the particle density ϱ_p and the particle volume V_p. The drop is also characterized by two quantities, e.g., the bulk density $\overline{\varrho}$ and the drop radius R. Alternatively, in the same way as for a single particle, the drop mass and the drop volume could be used instead. The force accelerating the suspension drop is characterized by the gravitational acceleration g. From these seven quantities any others can be derived, i.e., the number of (real) particles n_p^r, the ratio of particle radius to drop radius $\epsilon = r/R$, the initial particle volume fraction $\Phi = n_p^r \epsilon^3$, as well as the different dimensionless numbers discussed below. According to the Buckingham Π Theorem the number of independent dimensionless groupings fully characterizing the system is three less than the total number of variables (given mass, length, and time as base dimensions). Thus, we have to specify at least four dimensionless parameters. All others can be derived from those.

The drop Reynolds number is based on a characteristic drop settling velocity U_d and the drop radius R,

$$\mathrm{Re}_d = \frac{U_d R}{\nu}, \tag{7}$$

and reflects the ratio of inertial to viscous forces on the macroscopic length scale R of the suspension drop. Here, we follow Machu *et al.*[9] who define $U_d := (\overline{\varrho} - \varrho) R^2 g / (\varrho \nu)$ in analogy to the terminal settling velocity of a solid particle with density $\overline{\varrho}$ and radius R.

The particle Reynolds number is based on the terminal settling velocity of a single particle, $U_p = \tau_p g (1 - \varrho/\varrho_p)$, and the particle radius,

$$\mathrm{Re}_p = \frac{U_p r}{\nu} = \frac{2}{9}\frac{\epsilon^3}{\Phi}\mathrm{Re}_d. \tag{8}$$

The particle Reynolds number is required to be much less than unity for the equation of motion, Eq. (2), to be valid (Maxey and Riley[15]). It should be noted that, since the dimensionless parameters are coupled among each other, the drop Reynolds number cannot be made arbitrarily large without violating the particle Reynolds number restriction.

The Stokes number is the ratio of the particle response time to a characteristic time scale of the fluid motion. In accordance with Machu *et al.* we define

$$\mathrm{St} = \tau_p \frac{U_d}{R} = \frac{2}{9}\frac{\varrho_p}{\varrho}\epsilon^2 \mathrm{Re}_d. \tag{9}$$

In consequence of our assumption of very small particles, the Stokes number was kept well below unity throughout the simulations.

The Froude number reflects the ratio of inertial to gravitational forces and is defined here as

$$\mathrm{Fr} = \frac{U_d}{\sqrt{gR}}. \tag{10}$$

A very large Froude number means that inertia dominates over gravity on the macroscopic scale of the suspension drop.

For the numerical treatment the governing equations, Eq. (1)–(5), are cast in nondimensional form by relating the variables to some reference quantities. A reasonable choice is to use the drop settling velocity and the drop radius as the reference velocity and length scale, respectively, ($U_{ref} = U_d, L_{ref} = R$). For the sake of completeness the governing equations are restated in dimensionless form. All variables are now considered dimensionless, although not specifically labeled as such. The nondimensional particle equation of motion reads

$$\frac{dv_i(t)}{dt} = \frac{1}{\mathrm{St}}(u_i[\vec{Y}(t), t] - v_i(t)) - \frac{1}{\mathrm{Fr}^2}\left(1 - \frac{\varrho}{\varrho_p}\right)\delta_{i3}, \tag{11}$$

with gravity pointing in negative x_3 direction. For inertialess particles Eq. (11) assumes the form

$$v_i(t) = u_i(t) - \frac{\mathrm{St}}{\mathrm{Fr}^2}\left(1 - \frac{\varrho}{\varrho_p}\right)\delta_{i3}. \tag{12}$$

In several preliminary simulations both Eqs. (11) and (12) were used alternatively with only negligible differences found in the results. Unless otherwise mentioned Eq. (12) was used in the simulations presented. The nondimensional Navier–Stokes equation reads

$$\frac{\partial u_i}{\partial t} + u_m \frac{\partial u_i}{\partial x_m} = -\frac{\partial p}{\partial x_i} + \frac{1}{\mathrm{Re}_d}\frac{\partial^2 u_i}{\partial x_m \partial x_m} + f_i^{(p)} \tag{13}$$

with the particle source term

$$f_i^{(p)} = -\frac{\varrho_p}{\varrho}\frac{1}{\mathrm{St}}\sum_{j=1}^{n_p^r}(u_{i,j}(\vec{Y}) - v_{i,j})\delta(x_i - Y_{i,j}). \tag{14}$$

As mentioned above it is sufficient to specify four dimensionless parameters to fully characterize the settling suspension drop. We generally choose to specify Re_d, St, Fr, and ϱ_p/ϱ or Φ. If Eq. (12) is used only the dimensionless settling velocity $\mathrm{St}/\mathrm{Fr}^2$ needs to be given. In some cases we provide additional parameters such as the number of particles for clarity.

C. Numerical implementation

In order to solve the governing fluid equations a Fourier pseudospectral method is employed (see, e.g., Orszag[17] and Schumann *et al.*[18]). Each term in Eq. (13) is Fourier transformed. The resulting ordinary differential equation is discretized and numerically solved using a combined Runge–Kutta Crank–Nicolson scheme for the time integration. In this scheme the nonlinear terms are discretized according to a third-order Runge–Kutta scheme whereas the linear terms are implicitly treated using a second-order Crank–Nicolson scheme. The time step is computed according to a Courant–Friedrichs–Levy criterion (CFL). Continuity is ensured by projecting the velocity Fourier coefficients onto a

divergence-free basis. In order to avoid computationally expensive convolution sums the nonlinear terms are computed in real space rather than in Fourier space. Dealiasing according to the 3/2 rule is used to minimize errors associated with the nonlinear computation (see Canuto *et al.*[19]). The computational domain is a box of side length L with periodic boundaries. In each direction, x_1, x_2, x_3, N equidistant grid points are used to compose the Eulerian mesh. The particle equations, Eqs. (11) or (12), are solved in real space using the same Runge–Kutta scheme as for the fluid equation.

Since the computational domain contains no solid boundaries there is no mechanism that would prevent the particles and the fluid from ever more accelerating in the direction of gravity. To maintain the system in equilibrium a uniform pressure gradient is imposed in positive x_3-direction balancing the net weight of the particles per unit volume (Maxey and Patel[20]). Settling velocities are computed with respect to the mean fluid velocity in x_3-direction.

To compute the Stokes drag term in the particle equation, the fluid velocity is to be evaluated at the instantaneous particle locations. In most cases trilinear interpolation was used to this end. In order to study the influence of interpolation, fourth-order accurate Lagrangian polynomials as well as spectral summation were used alternatively (cf. Sec. IV). Interpolation is also needed to distribute the particles' feedback forces onto the Eulerian mesh. Unless otherwise mentioned the feedback force of a particle was distributed to the surrounding eight grid points by second-order accurate trilinear interpolation. Alternatively, top hat interpolation was used meaning that the full feedback force of a particle is entirely attributed to the closest grid point.

The simulation of a very large number of particles can be computationally too expensive to be accomplished. To circumvent this problem the point-particle approximation was augmented by introducing computational particles. Each computational particle is considered a representative of a cloud of particles, which are supposed to be in uniform motion with the computational particle. The number of computational particles can be chosen much smaller than that of real particles thus ensuring an acceptable computational time. The ratio of real to computational particles is denoted by

$$M = \frac{n_p^r}{n_p^c}, \tag{15}$$

where $M \geqslant 1$. With the concept of computational particles included the numerical algorithm described changes only slightly. Each computational particle is tracked along its trajectory according to Eq. (1) and Eq. (11) or (12). The two-way coupling term is altered such that the right-hand side of Eq. (14) is multiplied by M and the sum is evaluated over all computational particles n_p^c rather than all real particles n_p^r. For a more detailed discussion of computational particles the reader is referred to Elghobashi[21] or Druzhinin.[22]

At the beginning of a simulation the suspension drop is composed by randomly distributing n_p^c computational particles within a spherical boundary of radius R. The drop is placed in the center of the periodic computational box with the particles and the fluid being initially at rest. Unless otherwise mentioned the ratio of the box side length L to the initial drop radius R was $L/R=15$ in all simulations for moderate Reynolds numbers.

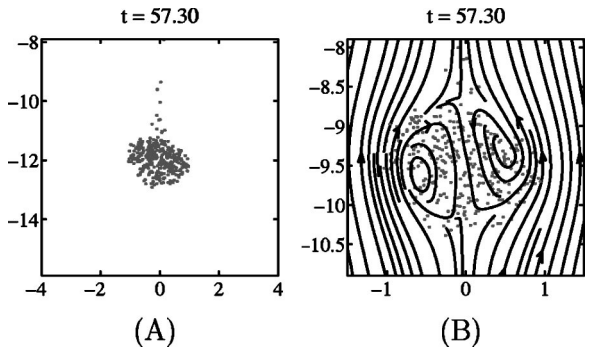

FIG. 1. Suspension drop settling at $\mathrm{Re}_d=0.1$. (A) Particles leak away into a tail emanating from the rear of the drop. (B) Streamlines in (x_1, x_3) plane at $x_2=0$ computed in a coordinate system moving with the drop's center of mass (zoomed in). St=0.035, Fr=1.414, $\Phi=0.02$, $n_p^c=n_p^r=320$, $L/R=8$, and $N=64$.

In the figures presented in the subsequent sections the particles' size may be larger than their actual size in the simulations and, if $n_p^c > 2000$, no more than 2000 particles will be shown for clarity. Also, the particle positions will be displayed with respect to a fixed coordinate system (nonperiodic x_3-coordinate) to indicate the distance traveled by the suspension drop. The initial position of the drop's center of mass coincides with the origin of this coordinate system.

III. VALIDATION: LOW REYNOLDS NUMBERS ($\mathrm{Re}_d \ll 1$)

For drop Reynolds numbers much less than unity the suspension drop as a whole settles under creeping flow conditions. Nitsche and Batchelor[8] (hereafter referred to as N&B) examined this case both numerically and theoretically. Here we use their results for comparison and validation of our numerical method. N&B found that the drop retains a roughly spherical shape while settling. Only a few particles leak away into a tail emanating from the rear of the drop. Inside the drop the particles undergo a circulatory motion similar to Hill's vortex. This behavior was exactly reproduced in our simulations. Figure 1 shows a suspension drop settling at $\mathrm{Re}_d=0.1$ (Reynolds numbers $\mathrm{Re}_d<0.1$ did not show any different results). The parameters were matched to one of the cases given by N&B in their Table I, i.e., $\Phi=0.02$, $n_p^c=n_p^r=320$, $\epsilon=0.0397$ (corresponding to St=0.035, Fr=1.414). The drop still has a coherent, roughly spherical structure and the tail of particles is clearly visible. This drop can be compared with that in Fig. 1(b) of N&B for $T=10$ (note their different definition of the dimensionless time). It shows good qualitative agreement. Sectional streamlines at $x_2=0$ (vertical box center plane) are also provided in Fig. 1. The fluid is subject to a circulatory motion directed downward near the drop's vertical center line and upward in the outer parts of the drop.

In the simulations of N&B the number of particles is confined to a maximum of 320, probably due to computer

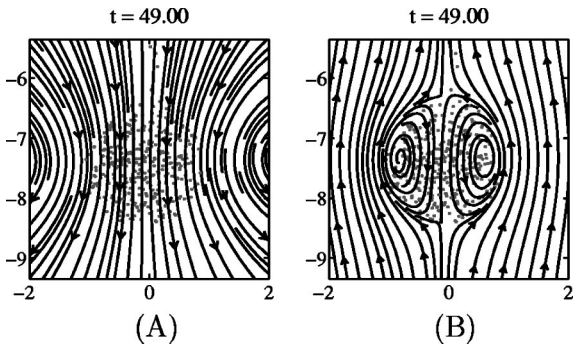

FIG. 2. Streamlines in (x_1,x_3) plane at $x_2=0$. Velocity computed in (A) a fixed coordinate system and (B) a coordinate system moving with the particles' center of mass. $\mathrm{Re}_d=0.01$, $\mathrm{St}=0.001$, $\mathrm{Fr}=0.447$, $\Phi=0.02$, $n_p^r=n_p^c=2095$, $L/R=8$, and $N=64$.

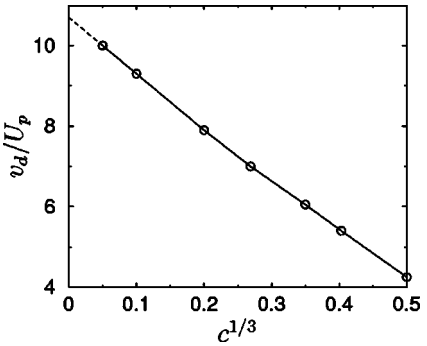

FIG. 3. Hindered settling of suspension drops. The drop settling velocity v_d is shown as a function of the drop volume concentration $c^{1/3}$. Circles indicate simulations performed. Dashed line extrapolates data to $c=0$.

limitations. A clearer picture of the underlying flow field structure is obtained when a larger number of (smaller) particles is used. The larger number of particles results in a finer discretization of the excess mass of the drop and a smoother drop "surface" (interface between clear fluid and suspension). Figure 2 shows an example of a suspension drop with 2095 particles settling at $\mathrm{Re}_d=0.01$ $(\mathrm{St}=0.001, \mathrm{Fr}=0.447, \varrho_p/\varrho=1000)$. The streamline plot of the velocity field is shown in both a fixed coordinate system and a relative one attached to the drop's center of mass. Here, the theoretical streamline pattern given by N&B in their Fig. 2 is very well reproduced. As long as a particle stays inside the region of closed streamlines it remains within the cohesive structure of the drop. However, if a particle settles close to the vertical center line it may get outside this region. When reaching the drop's lower boundary the particle may be pulled outside the region of closed streamlines as a result of fluid drag forces pulling it sideways and upward (following the streamlines) and gravity pulling it downward. Once outside the enclosing streamlines the particle is swept towards the rear stagnation point at the upper boundary and leaks away into the tail due to its reduced settling velocity outside the cohesive ensemble of particles (the settling velocity of a single particle is typically several orders of magnitude smaller than the settling velocity of the drop).

For a quantitative validation of our numerical approach we examined the drop settling velocity. It is important to recall that our numerical domain has periodic boundaries, i.e., a regular three-dimensional array of suspension drops is simulated rather than a single suspension drop in infinite fluid. As shown above the periodicity has essentially no effect on the principal features of the settling process and even the details, such as the internal circulatory fluid motion, are well reproduced. However, we found that the periodic boundaries do affect the drop's settling velocity. Each drop displaces fluid when settling downwards, which creates an upward flow in its vicinity affecting the neighboring drops. The overall effect is a decrease in settling velocity. A similar decrease in the settling velocity of irregular particle suspensions and regular arrays of solid particles has been reported in the literature and is usually referred to as the hindered settling effect, see, e.g., Sangani and Acrivos[23] and Zick and Homsy.[24]

The hindered settling of suspension drops is demonstrated in Fig. 3, where the dimensionless drop settling velocity v_d/U_p is shown as a function of the drop volume fraction $c=4/3\pi R^3/L^3$. The parameters for the simulations were matched to the N&B case with $\Phi=0.02$, $n_p^c=n_p^r=160$, $\epsilon=0.05$. Additionally, we specified $\mathrm{Re}_d=0.1$ (yielding $\mathrm{St}=0.056$, $\mathrm{Fr}=1.414$, $\varrho_p/\varrho=1000$). With increasing box size (decreasing c) the number of grid points was augmented accordingly in order to keep the flow field resolution inside the drop constant, i.e., the same ratio of grid points per drop radius in each direction. The larger the drop volume fraction the smaller is the distance between adjacent drops in the periodic array, which enhances the effect of decreasing velocity. For example, increasing the drop volume fraction from $c^{1/3}=0.1$ to $c^{1/3}=0.2$ causes the settling velocity to decrease by $\approx 15\%$. In Fig. 3 it is seen that the decrease in settling velocity is nearly linear for small drop volume fractions $c^{1/3}$. In the case of an array of solid spheres it can be shown analytically that, for small (sphere) volume fractions, the settling velocity depends roughly linearly on $c^{1/3}$ (Hasimoto,[25] Sangani and Acrivos[23]). Assuming that the same linear dependence applies to hindered settling of suspension drops, the data in Fig. 3 is linearly extrapolated to $c=0$, which corresponds to a suspension drop in infinite fluid. This yields a settling velocity $v_d^0/U_p=10.7$, which is in good agreement with the result by N&B (see Table I).

The drop settling velocity as a function of time is shown in Fig. 4 for the case of $c^{1/3}=0.2$. The drop is rapidly accelerated from rest to reach a quasistationary settling velocity for a short period of time between $t\approx 10$ and $t\approx 25$ (it is this time that was taken for the plot in Fig. 3). As soon as particles start leaking away into the tail the settling velocity slowly decreases.

TABLE I. Comparison of drop settling velocity with Nitsche and Batchelor (Ref. 8).

	N&B: theory	N&B: simulation	extrapolated (Fig. 3)
v_d^0/U_p	10.6	10.5 ± 0.1	10.7

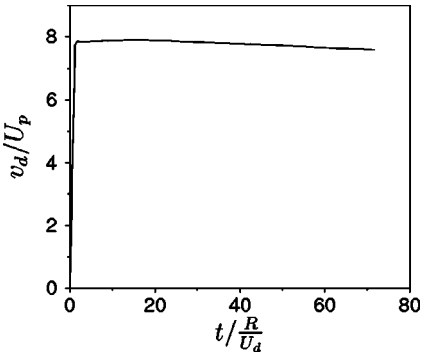

FIG. 4. Drop settling velocity as a function of time for $\mathrm{Re}_d=0.1$ and $L/R=8$ ($c^{1/3}=0.2$, cf. Fig. 3).

Figure 5 shows a comparison between hindered settling/rising of suspension drops, solid particles, and bubbles of the same size. In order to be independent of the individual drop (or particle/bubble) properties, the settling/rise velocities have been normalized by the corresponding terminal velocities in the limiting case of $c=0$. Thus, in principle, the curve for suspension drops shown in Fig. 5 should be independent of specific particle and drop properties as long as $\mathrm{Re}_d \leqslant 0.1$. Some spurious effects may be present due to the coarse drop discretization in terms of the number of particles ($n_p^c=160$). The principal observation is that the hindered settling of a regular array of suspension drops is less pronounced than that of solid particles and more pronounced than the hindered rising of bubbles. The analytical results for hindered settling of liquid drops and porous particles can be found in Sangani[26] and Mo and Sangani.[27] Based on the formula for liquid drops (including the limiting case of bubbles) presented in the former work, the hindered settling of suspension drops can be approximated for small drop volume fractions by

$$\frac{v_d}{v_d^0}=1-1.76c^{1/3}\frac{U_t}{v_d^0}, \tag{16}$$

where the terminal velocity of a solid particle of the same size as the suspension drop is $U_t=(2/9)\ U_d=(2/9)(\overline{\varrho}-\varrho)R^2g/\mu$. Equation (16) is also plotted in Fig. 5 and found

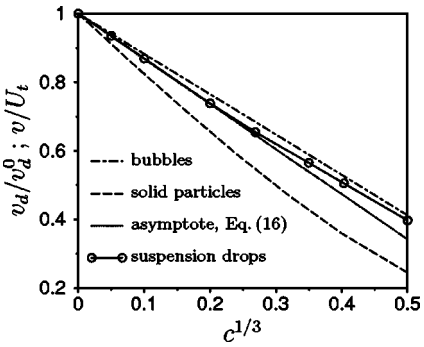

FIG. 5. Hindered settling/rising of suspension drops, solid particles, and bubbles. The drop settling velocity v_d is normalized by the extrapolated settling velocity v_d^0. The particle and bubble velocities v are normalized by their corresponding terminal (Stokes) velocities U_t in infinite fluid. The asymptote is an approximation for small c according to Eq. (16).

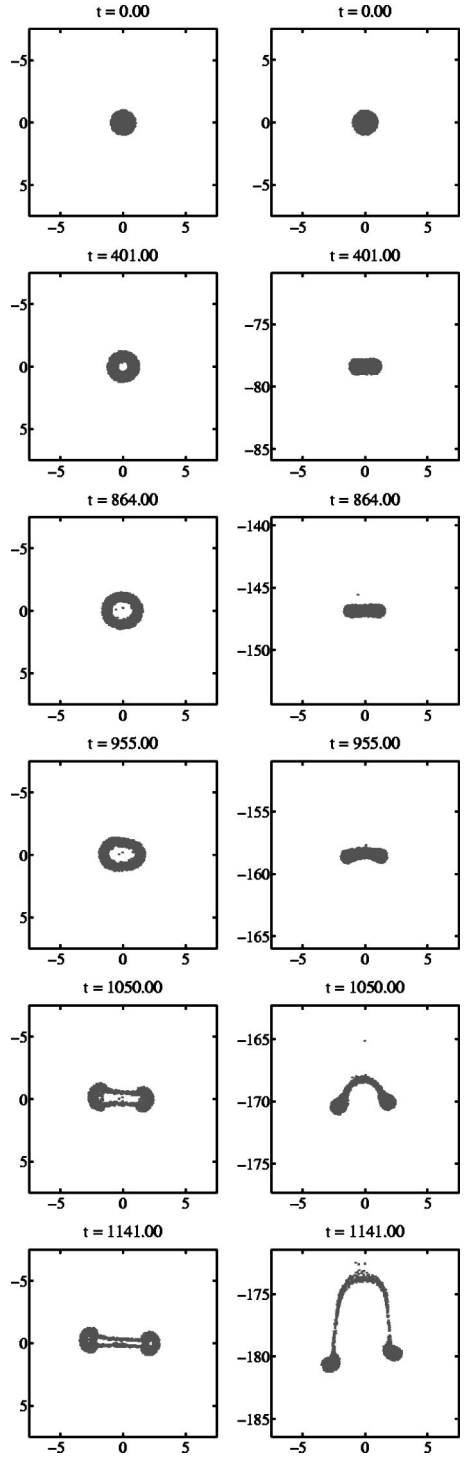

FIG. 6. Typical sequence of deformations and breakup of a suspension drop settling at $\mathrm{Re}_d=1$ ($\mathrm{St}=0.0076$, $\mathrm{Fr}=4.47$, $\varrho_p/\varrho=1000$, $n_p^c=n_p^r=100\,096$, $N=128$). Left, top view; right, side view.

to accurately describe the asymptotic behavior of suspension drops for drop volume fractions $c^{1/3} \lesssim 0.2$.

IV. RESULTS: MODERATE REYNOLDS NUMBERS ($1 \leqslant \mathrm{Re}_d \leqslant 100$)

A. Reynolds number dependence

At drop Reynolds numbers $\mathrm{Re}_d \geqslant 1$ the suspension drop undergoes a complex shape evolution with eventual breakup into a number of secondary blobs. Figure 6 shows a typical

FIG. 7. Disintegrated suspension drop (left) and liquid drop (right) in an experiment by Machu *et al.* (Ref. 9).

sequence of deformations and breakup of a drop settling at $\mathrm{Re}_d=1$ ($\mathrm{St}=0.0076$, $\mathrm{Fr}=4.47$, $\varrho_p/\varrho=1000$). The initially spherical drop flattens into an oblate shape featuring a growing dimple at its rear (for $t\lesssim 280$, not shown in the figure). The dimple is formed because the fluid inside the drop below the particles at the rear (upper) boundary is accelerated downward by particle drag, whereas the fluid in front of the drop is still quiescent. Thus, the particles at the rear settle faster than those at the leading front, which creates the dimple shape. The dimple keeps growing inside the drop such that the latter deforms into a torus. The torus grows larger in diameter while traveling, before it eventually becomes unstable and disintegrates into two secondary blobs. The last sample of the sequence in Fig. 6 looks remarkably similar to two photographs of experiments at low Reynolds numbers given by Machu *et al.*, which are shown in Fig. 7. In the experiments the initial conditions were certainly different from a spherical suspension drop with all particles at rest. However, the key feature of the breakup process, the formation of a torus as found in our simulation, was observed in the experiments as well. A detailed discussion of the influence of initial conditions will be given later in Sec. I.

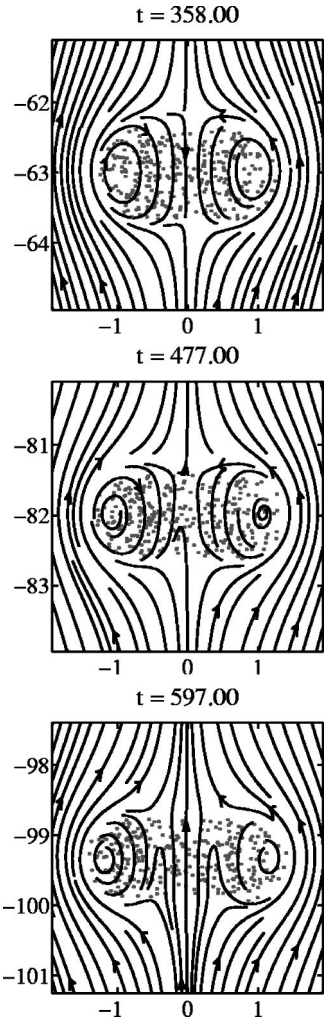

FIG. 8. Transition from closed to open torus for $\mathrm{Re}_d=1$. Same simulation as shown in Fig. 6. The streamlines are computed in a coordinate system moving with the drop's center of mass and are displayed on a vertical plane at $x_2=0$. For clarity only 300 particles are shown.

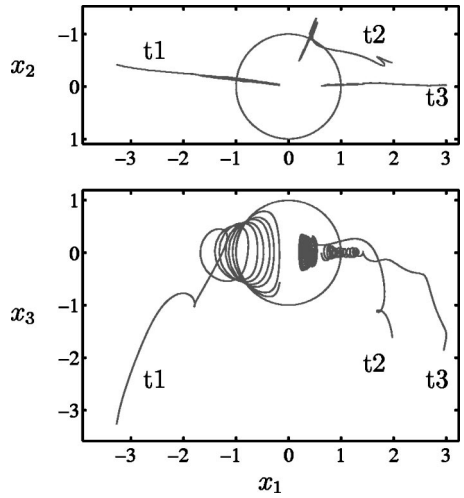

FIG. 9. Trajectories of three particles ($t1,t2,t3$) inside the suspension drop shown in Fig. 6 ($\mathrm{Re}_d=1$). The circle indicates the initial drop. The trajectories are computed in a coordinate system attached to the particles' center of mass.

Figure 8 shows a visualization of the flow field inside and outside the settling torus from Fig. 6. The streamlines, displayed on a vertical plane through the center of the computational box ($x_2=0$), reveal a ring vortex growing in diameter over time. The ring vortex coincides with the particles forming the settling torus. At $t=358$ the ring vortex is closed in the sense that no streamlines pass from the front (lower) stagnation point through its center to the rear (upper) stagnation point. At $t=477$, due to the growing ring hole, fluid starts penetrating the torus from the front stagnation point. At $t=597$ an open ring vortex is observed with streamlines passing through the center hole. This marks the beginning of torus disintegration. The transition from a closed to an open torus was observed by Machu *et al.* in both their experiments and simulations. The difference is that they considered a low Reynolds number case, $\mathrm{Re}_d\ll 1$, with an initially bell-shaped drop whereas here, the same phenomenon occurs for $\mathrm{Re}_d=1$ and an initially spherical drop. As will be shown later in this section, the transition from a closed to an open torus is not observed for Reynolds numbers of about 100.

Figure 9 shows the trajectories of three particles in a frame moving with the particles' center of mass for the same case of $\mathrm{Re}_d=1$ discussed above. At the beginning the particles undergo a circulatory motion essentially the same as that indicated by the streamlines in Fig. 8. As long as the torus is stable the circulation continues and, as seen in the

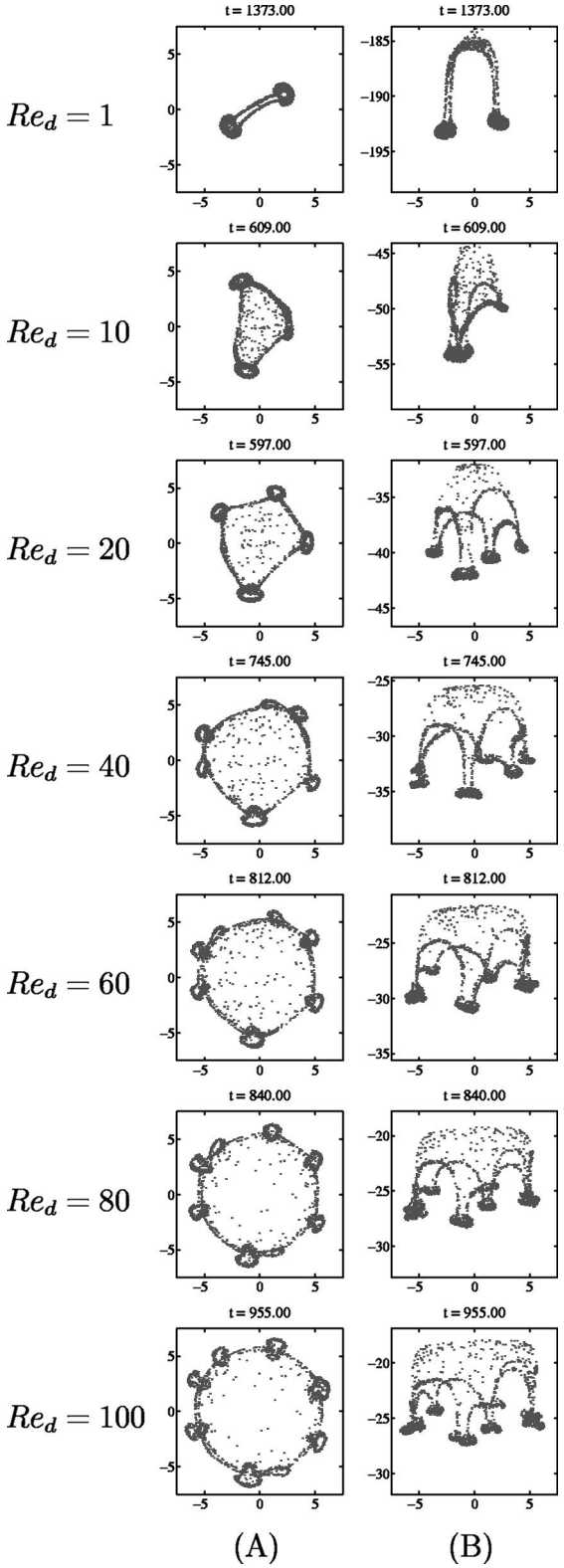

FIG. 10. Disintegrated suspension drops at different drop Reynolds numbers. (A) Top view, (B) side view. $\mathrm{St}_d = 0.01$, $\mathrm{Fr} = 10$, $\phi = 0.02$, and $n_p^c \approx 108\,000$.

top view of Fig. 9, the particles are not displaced in azimuthal direction of the torus. This indicates that the flow field remains axisymmetric with respect to the x_3 axis. Only when the bulges form and the torus starts disintegrating (cf. $t = 955$, Fig. 2), particles are entrained towards the blobs being formed (trajectory $t2$).

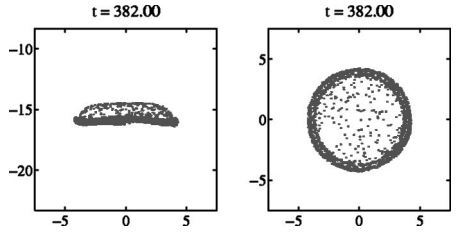

FIG. 11. Side and top view of the torus spanned by a "membrane" of dilute particles at $\mathrm{Re}_d = 100$.

In order to study the Reynolds number dependence of the disintegration process, the Reynolds number Re_d was successively increased while keeping (almost) all other parameters constant. We chose $\mathrm{St} = 0.01$, $\mathrm{Fr} = 10$, $\Phi = 0.02$, $n_p^c \approx 108\,000$, $M = 7$, and the same initial particle distribution in all cases. From Eq. (9) it is clear that the density ratio has to be decreased accordingly if the Stokes number is to remain constant with increasing Re_d. The grid resolution was set to $N = 128$.

Figure 10 shows disintegrated suspension drops for $\mathrm{Re}_d = 1$, 10, 20, 40, 60, 80, and 100. It is observed that the number of secondary blobs increases with increasing Reynolds number. For $\mathrm{Re}_d = 1$ two secondary blobs are obtained, for $\mathrm{Re}_d = 100$ the torus breaks up into seven major and one minor secondary blobs. The shape evolution of the initially spherical drop and the torus before breakup is similar to that shown in Fig. 6 in all cases. However, for $\mathrm{Re}_d > 1$ the torus is usually spanned by a "membrane" of dilute particles as shown in Fig. 11.

A comparison of the (nondimensional) drop settling velocities for different Reynolds numbers is provided in Fig. 12. It must be emphasized that the settling velocities are inherently affected by the hindered settling effect discussed in the previous section. Therefore, the velocities have been normalized by the maximum settling velocity for $\mathrm{Re}_d = 1$. This allows for a relative comparison between different Reynolds numbers. It is seen that the higher the Reynolds number the smaller are the settling velocities. After reaching a peak value shortly after the particles are released the settling velocities decrease gradually as the torus is forming and expanding. This decrease is stronger and occurs at increasingly shorter times for larger Reynolds numbers reflecting a faster

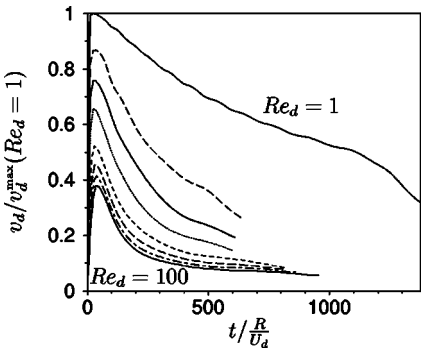

FIG. 12. Comparison of drop settling velocities for different Reynolds numbers, $\mathrm{Re}_d = 1, 5, 10, 20, 40, 60, 80, 100$ (Re_d successively increasing from top down). Same simulations as in Fig. 10.

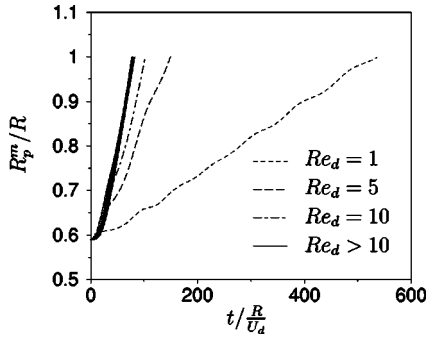

FIG. 13. Time evolution of the mean radial particle distance from the center of mass R_p^m for different Reynolds numbers, $\mathrm{Re}_d = 1, 5, 10, 20, 40, 60, 80, 100$. Same simulations as in Fig. 10.

disintegration. For $\mathrm{Re}_d = 1$ the decrease of the settling velocity is considerably weaker than in the other cases. This is due to a relatively slow deformation of the drop into a torus, which then remains stable for a long period of time. Towards $\mathrm{Re}_d = 100$ the velocity curves become similar suggesting an asymptotic behavior for $\mathrm{Re}_d = O(100)$. In order to determine the time required for the drop to deform into a torus, we define a radius R_p^m as the mean distance of the particles to the center of mass in the (x_1, x_2) plane. The time T_{d-t} required for R_p^m to reach the initial drop radius R is taken as a characteristic measure for the deformation of the drop into a torus. Figure 13 shows the time evolution of R_p^m/R until $R_p^m/R = 1$ for different Reynolds numbers. The corresponding characteristic times T_{d-t}, normalized by $T_{d-t}(\mathrm{Re}_d = 1)$, are given in Table II. The principal observation is that the deformation of the drop into a torus occurs the faster the higher the Reynolds number. Again, towards $\mathrm{Re}_d = 100$ an asymptotic behavior is found. In the case of $\mathrm{Re}_d = 1$ the time evolution of R_p^m reveals a slightly pulsating expansion and contraction of the torus. This behavior was also observed by Machu *et al.* for vanishing Reynolds number and a pearlike initial drop shape.

Figure 14 shows the time evolution of the flow field for a suspension drop settling at $\mathrm{Re}_d = 100$. The streamlines are computed in a coordinate system moving with the particles' center of mass. They are shown on a vertical center plane at $x_2 = 0$. As opposed to the case of $\mathrm{Re}_d = 1$ the particle torus and the ring vortex do not coincide and the corresponding transition from a closed to an open torus is not observed. Instead the circulatory motion inside the initial drop starts extending towards the rear of the flattening drop shortly after the release ($t = 95$). As the drop deforms into a torus spanned by a membrane of particles, the ring vortex moves completely outside the torus and the streamline structure looks similar to the wake of a circular flat plate ($t = 191$). As long as the torus and the ring vortex coincide at least partially, the streamlines at the rear (upper boundary) of the torus point towards the torus. This keeps the torus and the membrane a compact structure. When the ring vortex detaches from the torus, however, the membrane of particles starts bulging towards the rear ($t = 286$). This is due to the smaller settling velocity of single particles within the membrane compared to the settling velocity of the compact torus. In the further course of the settling process the ring vortex gradually dissipates ($t = 382$). Since the particle torus and the ring vortex no longer coincide, there is no particle-fluid interaction that could sustain the vortex and the latter eventually disappears completely ($t = 477$).

As pointed out by Machu *et al.* and others (e.g., Joseph and Renardy[28]) the disintegration of the suspension torus is due to a Rayleigh–Taylor-type instability. In fact, in a first approximation the suspension can be considered a pseudoliquid of increased density $\overline{\varrho}$. In this case small perturbations of the interface between the heavier pseudoliquid making up the torus and the lighter clear fluid will amplify and eventually lead to breakup. For a detailed discussion of the classic Rayleigh–Taylor instability the reader is referred to Chandrasekhar.[29] In the case of a "real" suspension, i.e., a particle-fluid mixture as in our simulations, there is no distinct interface between torus and clear fluid, but the instability mechanism works in a similar way as for two fluids of different density. A not perfectly uniform particle distribution results in a locally varying mixture density of the suspension, which causes some parts of the torus to settle faster than others. This creates perturbations of the torus shape and "surface" and is the starting point of the instability mechanism.

In the following sections we address the question: What determines the breakup behavior of a suspension drop at a given Reynolds number? To this end we study the influence of the initial particle positions, the effect of initially imposed drop shape perturbations, as well as the influence of the drop mass discretization in terms of the number of particles. With respect to the instability leading to torus breakup we try to distinguish as clearly as possible between perturbations of a "physical" nature, which are our primary interest, and those of a "numerical" nature. The former can also be present in a real-world experiment, whereas the latter are inherent to the numerical procedure. It is important to distinguish between "physical" and "numerical" sources of perturbations because both may affect the breakup behavior of a suspension drop in numerical simulations. Therefore, in order to demonstrate that our results are not tainted by numerical effects, the influence of the grid resolution, the periodic boundaries, and the interpolation used in the computation of the particle feedback force will be discussed briefly.

1. Influence of the initial particle distribution

The crucial role of the initial conditions has been pointed out by several authors (e.g., Machu *et al.*,[9] Kojima *et al.*[10]),

TABLE II. Characteristic times T_{d-t} for the deformation of the drop into a torus.

Re_d	1	5	10	20	40	60	80	100
$T_{d-t}/T_{d-t}(\mathrm{Re}_d = 1)$	1	0.278	0.190	0.154	0.146	0.144	0.146	0.149

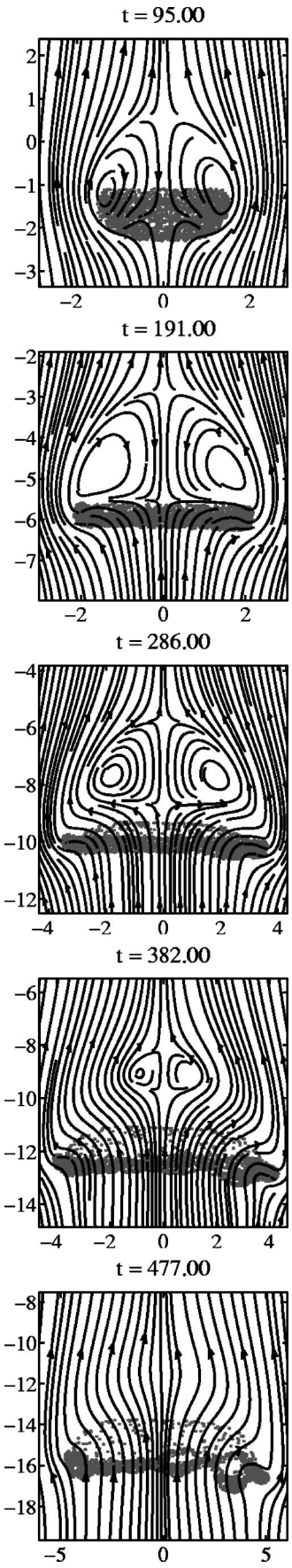

FIG. 14. Evolution of the flow field for a suspension drop settling at $\mathrm{Re}_d = 100$. The streamlines are computed in a coordinate system moving with the drop's center of mass and are displayed on a vertical plane at $x_2 = 0$. From top to bottom the view frame zooms out of the expanding suspension torus.

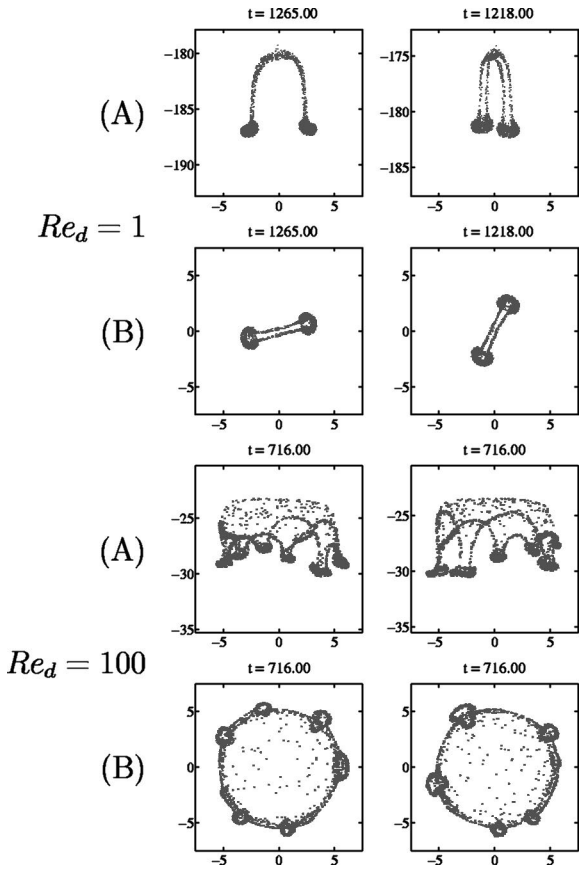

FIG. 15. Disintegrated blobs for different initial particle positions. (A) Side view, (B) top view. Top, $\mathrm{Re}_d = 1$, St=0.01, Fr=4.5, $\varrho_p/\varrho = 1000$; bottom, $\mathrm{Re}_d = 100$, St=0.01, Fr=44.7, $\varrho_p/\varrho = 1000$. $N = 64$ in both cases.

primarily with respect to the initial drop shape. Machu *et al.* showed that even at very low Reynolds numbers $\mathrm{Re}_d \ll 1$ an initial shape different from a sphere, for example, a bell-shaped drop, deforms into a torus with subsequent breakup. We found that the particle positions within the initial drop also affect the details of the breakup process and may even yield a different number of secondary blobs. Figure 15 shows two examples of simulations with different initial particle positions. The initial distribution was uniformly random in all cases. For $\mathrm{Re}_d = 1$ the number of secondary blobs did not vary for different initial particle positions, but the location of the blobs was different. For $\mathrm{Re}_d = 100$ the details of the particular breakup pattern were different for different initial particle positions and even the number of secondary blobs varied between five and seven. These results demonstrate that the instability is very sensitive to the details of the initial conditions, and corroborate the idea of the particle distribution being the primary source of perturbations.

In order to shed more light on the role of the particle distribution, a set of simulations was performed with initially perturbed drop shapes. Perturbations due to the (initial) particle distribution are termed "natural" in the following, whereas the initial shape variations are called "imposed artificial" perturbations. Starting from a spherical shape with a uniformly random particle distribution, the particles' radial position with respect to the drop center line in the vertical direction was shifted according to

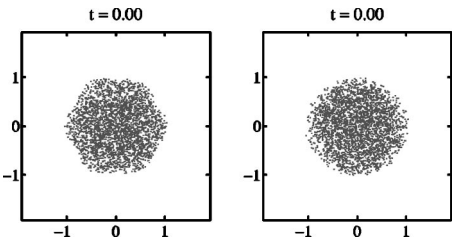

FIG. 16. Initially perturbed suspension drop. Top view (left), side view (right). $A_s=0.005R$, $l_s=6$.

$$\Delta r = A_s \cos(l_s \theta). \tag{17}$$

Here Δr is the radial shift of the particle position in the (x_1, x_2) plane with respect to the drop center line, A_s is the perturbation amplitude, l_s is the number of periods along the circumference, and θ is the azimuthal angle. Figure 16 displays an initially perturbed suspension drop. Clearly, this is only one possibility to introduce controlled (artificial) perturbations allowing us to trigger a certain breakup behavior of the suspension drop.

Figure 17 shows disintegrated, artificially perturbed drops with $l_s=6$ ($\mathrm{Re}_d=100$, $\mathrm{St}=0.01$, $\mathrm{Fr}=44.7$). The perturbation amplitude A_s was varied between $0.1R$ and $0.001R$. The last drop shown in the lower two rows is an unperturbed reference case. The number of particles was $n_p^c=29433$ resulting in an initial mean particle spacing of $d\approx 0.052R$ [defined as $d=(4\pi/3n_p^c)^{1/3}R$]. If the artificial perturbation level is large enough, the forced perturbations dominate the disintegration process and the drop breaks up into six equally spaced secondary blobs (first and second case with $A_s=0.1R$ and $A_s=0.05R$). If the artificial perturbation amplitude drops well below the order of the mean particle spacing ($A_s=0.001R$), the natural perturbations clearly predominate and the disintegrated structure differs only little from the unperturbed reference case. Between these two cases, the natural and the artificial perturbation level are apparently of about the same order and none clearly prevails ($A_s=0.01R$). Here, as in other parts of the paper also, we rely on visual judgment only, primarily for lack of measurable quantities that better characterize the entire breakup process.

As long as the artificial perturbations are large enough, i.e., of the order of the mean particle spacing, different breakup patterns can be triggered depending on the parameter l_s. For $\mathrm{Re}_d=100$ any number between three and ten secondary blobs could be forced (same parameters as in Fig. 17, $A_s=0.05R$). Three examples are shown in Fig. 18. These results further illustrate the crucial role of the particle distribution as a source of perturbations. The interplay of natural and artificial perturbations will be revisited within the spectral analysis of the settling torus in Sec. IV B.

2. Influence of the number of particles

The excess mass of the suspension drop with respect to the surrounding clear fluid is concentrated into the points where the particles are located. In this sense the drop can be regarded as discretized in terms of the number of particles making up the suspension. Now we focus on the question

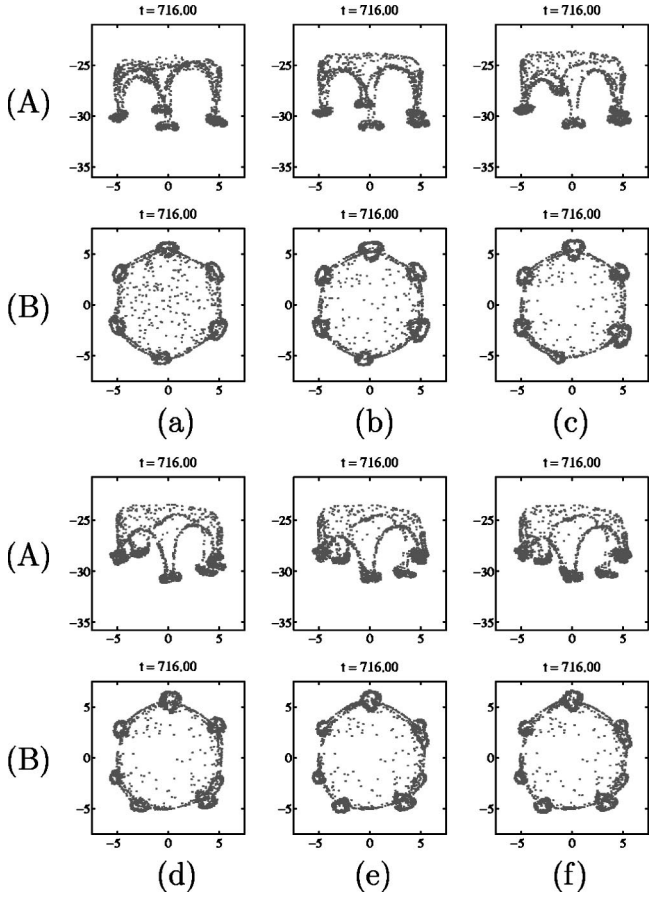

FIG. 17. Disintegrated initially perturbed drops. $\mathrm{Re}_d=100$, $\mathrm{St}=0.01$, $\mathrm{Fr}=44.7$, $\varrho_p/\varrho=1000$, $n_p^c=29433$, $M=2251$, $N=64$, and $l_s=6$. (A) Side view, (B) top view; (a) $A_s=0.1R$, (b) $A_s=0.05R$, (c) $A_s=0.025R$, (d) $A_s=0.01R$, (e) $A_s=0.001R$, and (f) unperturbed reference case. Initial mean particle spacing $d\approx 0.052R$.

how this drop discretization affects the breakup behavior of the suspension drop by varying the number of particles. The same integral drop properties, such as the bulk density and the particle volume fraction, can be realized by either a large number of small particles or a smaller number of larger particles. Thus, a different drop discretization in terms of the number of real particles involves different particle properties, e.g., the Stokes number increases with the particle radius under otherwise same conditions. For the case of $\mathrm{Re}_d=100$ a set of simulations was performed with an increasing number of real (and computational) particles. Since for $\mathrm{Re}_d=100$,

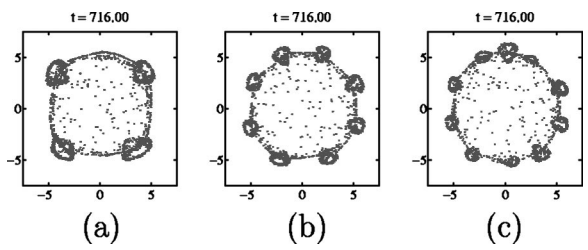

FIG. 18. Forced number of secondary blobs of (artificially) perturbed suspension drops, $\mathrm{Re}_d=100$, $\mathrm{St}=0.01$, $\mathrm{Fr}=44.7$, $\varrho_p/\varrho=1000$; (a) $l_s=4$, (b) $l_s=8$, (c) $l_s=10$; $A_s=0.05R$ in all cases. Natural (unperturbed) breakup into six major secondary blobs as in Fig. 17(f). $N=64$.

TABLE III. Number of computational and real particles and Stokes number for simulations with varying drop mass discretization. $\mathrm{Re}_d=100$, Fr=44.7, $\Phi=0.02$, and $M=130$.

n_p^c	509 645	2×10^6	4×10^6
n_p^r	$\approx66\times10^6$	260×10^6	520×10^6
St	0.01	0.004 06	0.002 53

$\mathrm{St}\leqslant0.01$, and $\Phi=0.02$ the resulting numbers of real particles are very large (of order 10^8) we chose a fixed $M=130$. The Froude number was Fr=44.7 in all cases. Table III shows the different parameters.

Figure 19 shows the results. It is observed that the number of secondary blobs increases with an increasing number of particles used in the simulation. There are two effects of a finer initial drop discretization: (i) the excess mass of the suspension is more uniformly distributed throughout the drop, and (ii) the (natural) perturbations introduced by the discrete particle distribution extend to a smaller length scale due to a decreased mean particle spacing. Consequently, the torus remains stable for a longer period of time, the visible breakup sets in at a later time (note the times given in Fig. 19 for the fully disintegrated drops). Comparison of the top views of cases (a) and (c) in Fig. 19 also reveals that the diameter of the disintegrated torus is larger in case (c), which provides additional room for a larger number of secondary blobs. It is concluded that for $\mathrm{Re}_d=100$ an increased number of real (and computational) particles, i.e., a finer drop discretization, results in a larger number of secondary blobs due to a delayed torus breakup.

A similar set of simulations with an increasing number of computational particles was performed for $\mathrm{Re}_d=1$. In this case the torus always breaks up into only two secondary blobs independently of the number of particles. This suggests that the range of possible disintegration patterns featuring a certain number of secondary blobs increases with increasing Reynolds number.

It is worth noting that the concept of computational particles offers a second possibility to examine the effect of a refined drop discretization. Instead of choosing a fixed ratio M, the number of computational particles can be augmented while keeping the number of real particles constant. The ratio M has to be adjusted accordingly. In this case the particle properties do not change and it is obvious that this situation could not be reproduced in a real-world experiment. However, the effect of a finer drop mass discretization as "seen by the fluid" can as well be studied this way. We conducted a set of simulations with the number of computational particles successively increased from about 5×10^5 to 4×10^6 and a fixed number of real particles $n_p^r\approx6.625\times10^7$ ($\mathrm{Re}_d=100$, St=0.01, Fr=44.7, $N=128$). The results revealed the same effect of a refined drop discretization as shown before. The torus disintegration is delayed resulting in an increased number of secondary blobs.

The findings discussed above necessitate a comment on the comparison between experiments and simulations. In a real-world experiment, in which a suspension drop is released into (roughly) quiescent fluid, the initial perturbations are not known. The particle distribution inside the suspension drop will certainly not be perfectly uniform and the drop will not have a perfectly well defined shape. Moreover, it is likely that other perturbations introduced by the apparatus to release the suspension drops (whatsoever its functional details) will be present. Thus, it is virtually impossible to match experimental and numerical conditions. Numerical simulations can predict a range of secondary blobs to be expected and possible breakup patterns. For example, in the case of $\mathrm{Re}_d=100$ it is likely to obtain approximately six secondary blobs. This number, however, may vary significantly in a real-world experiment due to unknown perturbations and different initial conditions.

The strong sensitivity of the instability to the details of the initial conditions is a notable characteristic of the drop disintegration process. As already mentioned the growing perturbations in our simulations may not only be of a "physical" nature, such as a not perfectly homogeneous particle distribution, but also due to numerical effects. In the remaining part of this section numerical influences are shown to be negligible thus confirming the results presented above.

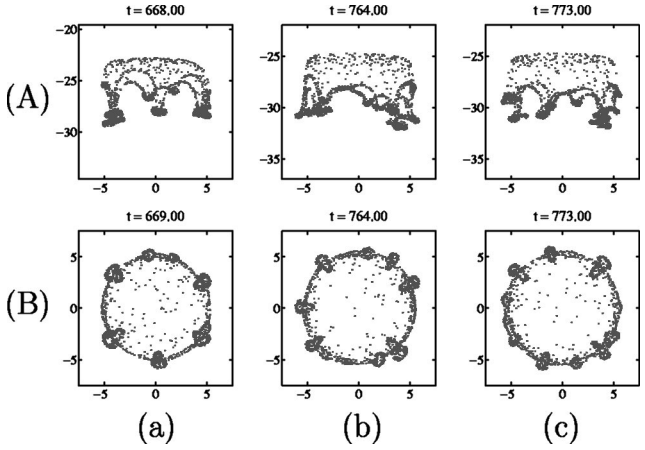

FIG. 19. Influence of the number of computational particles. (A) Side view, (B) top view of disintegrated drops; (a) $n_p^c=509645$, (b) $n_p^c=2\times10^6$, (c) $n_p^c=4\times10^6$. $\mathrm{Re}_d=100$, Fr=44.7, $M=130$, and $N=128$ in all cases.

3. Influence of the periodic boundaries

As has been shown for the low Reynolds number case, $\mathrm{Re}_d=0.1$, the periodic boundaries have a considerable effect on the drop settling velocity (hindered settling). Thus, it might be expected that they affect the breakup process in some general way such that, for example, the number of secondary blobs is influenced by the periodic boundaries. On the other hand, the substructural effects of the particle-fluid interaction, the internal circulating motion, was well reproduced in the low Reynolds number case despite the periodic boundaries. This would suggest only a minor influence of the periodicity on the disintegration process. Figure 20 shows disintegrated drops from two simulations with different interdrop spacings under otherwise same conditions ($\mathrm{Re}_d=100$, St=0.01, Fr=44.7, $\varrho_p/\varrho=1000$, $n_p^c\approx10^5$, same initial particle distribution). In the first case 128^3 grid points were used with $L/R=15$, in the second case 256^3 grid points with

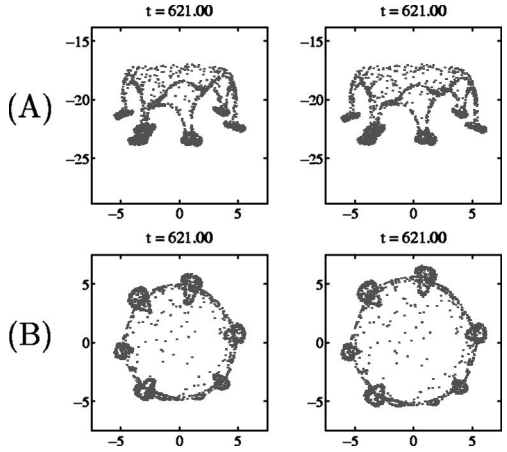

FIG. 20. Influence of periodic boundaries. Two simulations at $\mathrm{Re}_d=100$ (St=0.01, Fr=44.7, $\Phi=0.02$) with the same initial particle distributions but different interdrop spacing. (A) Side view, (B) top view. Left, $L/R=15$, $N=128$; right, $L/R=30$, $N=256$. The ratio of grid points per drop radius was equal in both simulations.

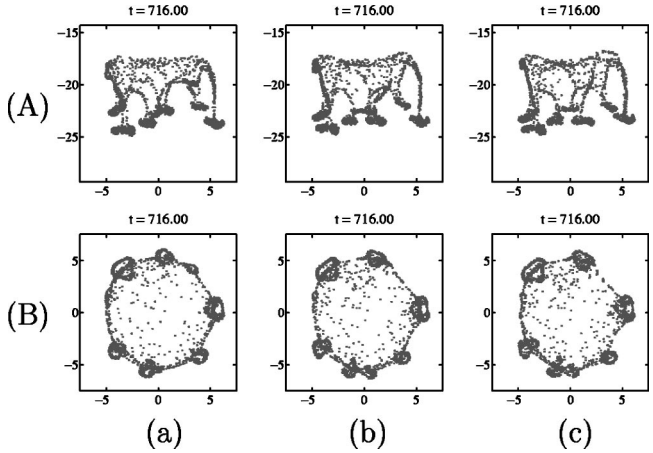

FIG. 21. Influence of interpolation: (A) trilinear fluid interpolation, (B) fourth-order Lagrange-polynomial fluid interpolation, and (c) spectral summation. In all cases trilinear interpolation of the particle feedback force was used. $\mathrm{Re}_d=100$, St=0.01, Fr=44.7, $\varrho_p/\varrho=1000$, $n_p=7337$, $M=9030$, and $N=64$.

$L/R=30$. The higher grid resolution in the second case ensures a fixed drop resolution in terms of grid points per drop radius. The disintegrated torus looks very similar in both cases. Not only is the same number of secondary blobs obtained, but also the details are very similar. It is concluded that the periodic boundaries have a negligible effect on the breakup pattern of the suspension drop. Thus, the Reynolds number dependence and the role of the particle distribution discussed above should as well apply to the general case of a single suspension drop in infinite fluid.

4. Influence of interpolation

Interpolation is used to compute the fluid velocity at the instantaneous particle positions and to distribute the particles' feedback force from the particle positions to the grid points of the Eulerian mesh. There are several studies available in the literature that examine the influence of interpolation in detail, primarily in turbulent particle-laden flows (e.g., Yeung and Pope,[30] Balachandar and Maxey,[31] Sundaram and Collins,[32] Kitagawa *et al.*[33]). Here, we confine ourselves to demonstrating that the use of different interpolation methods does not significantly alter our results of suspension drop disintegration at moderate Reynolds numbers. For the fluid interpolation three different methods were employed: (i) trilinear interpolation, (ii) fourth-order Lagrange polynomials, and (iii) spectral summation. These were used alternatively in a set of simulations with otherwise same parameters ($\mathrm{Re}_d=100$, St=0.01, Fr=44.7, $\varrho_p/\varrho=1000$, $n_p^c=7337$, $M=9030$). The grid resolution was set to $N=64$. In all cases linear interpolation was used to distribute the particle feedback force to the surrounding grid points. In the case of spectral summation a third-order accurate Runge–Kutta scheme was employed for both the linear and nonlinear terms (instead of a combined Runge–Kutta Crank–Nicolson scheme). Thus, the overall accuracy of the time integration was augmented from second to third order.

The results are shown in Fig. 21. The hardly visible differences between cases (b) and (c), i.e., Lagrange and spectral interpolation, respectively, are negligible. In the linear case (a) the number of secondary blobs is the same as in (b) and (c), however, their location is somewhat different. The principal features of the settling process, such as torus formation and breakup, are well captured in all three cases. Given the increased computational cost of Lagrange polynomial interpolation and spectral summation, it is reasonable to resort to linear interpolation. It should be noted that the influence of interpolation is significantly reduced if higher grid resolutions are used, e.g., $N=128$ as in the simulation shown in Fig. 6.

We also used first-order top hat interpolation to distribute the particle feedback force between the grid points. Here, the full feedback force of a particle is attributed to the closest grid point in its vicinity. The results did not show any major differences to those presented in Fig. 21.

5. Influence of the grid resolution

In numerical simulations reliable results are generally required to be independent of the grid resolution (grid convergence). To find a grid resolution fine enough to capture all relevant details of the disintegration process, a set of simulations with different numbers of grid points was performed. Figure 22 shows examples for $\mathrm{Re}_d=100$. It was found that a resolution of 64^3 grid points is sufficient to capture all characteristic features of the settling and disintegration process, i.e., torus formation and breakup into a certain number of blobs depending on the Reynolds number. However, it is worth noting that grid convergence in a strict sense is not given. The instability is very sensitive to only small perturbations of the suspension torus. A different grid resolution involves different relative positions between particles and grid points resulting in a slightly different particle feedback force. This small difference is sufficient to produce different details of the disintegrating torus. For example, the location of the secondary blobs along the torus' circumference may be slightly different in one simulation with $N=64$ and another one with $N=128$ and otherwise same parameters. Also,

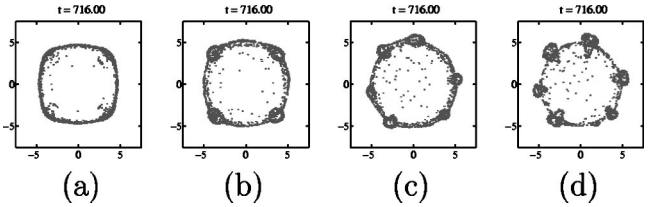

FIG. 22. Disintegrated blobs computed with different grid resolutions. From left to right: $N=16$, $N=32$, $N=64$, and $N=128$. $\mathrm{Re}_d=100$.

the disintegration process tends to evolve a little more slowly when using 64^3 grid points compared to 128^3.

B. Spectral analysis of settling drop and torus

The initial particle distribution has been identified as the primary source of perturbations, which are crucial to the instability developing during the drop settling process. To gain a deeper understanding of the particle dispersion processes involved, the particle field inside the settling drop and torus was analyzed from a spectral point of view. To this end the particle field was divided into N_s radially symmetric segments in the (x_1,x_2) plane according to the sketch in Fig. 23. The segments are similar to the slices of an orange. This segmentation served as a tool to study the time evolution of the particle distribution.

The idea is to define a measurable quantity $q(\theta_s,t)$ as a function of the (discrete) segmentation angle θ_s and time t and to study the time evolution of the Fourier coefficients associated with this quantity. Each segment contains a number of particles $n_p^s(\theta_s,t)$ that may change during the disintegration process. As will be demonstrated in the following, it is instructive to use this number as the time-dependent quantity, $q(\theta_s,t):=n_p^s(\theta_s,t)$. The number of particles per segment indicates whether particles accumulate in certain azimuthal regions. Another choice would be to use the mean particle settling velocity per segment, $q(\theta_s,t):=v_3^s(\theta_s,t)$, which may indicate whether particles settle faster in certain regions.

A reasonable number of segments N_s must meet two criteria: (i) the size of a segment should be much smaller than the smallest scale of particle clustering to be captured along the torus' circumference; (ii) a segment should contain enough particles such that n_p^s does not change significantly if the segment is slightly shifted in azimuthal direction. This is

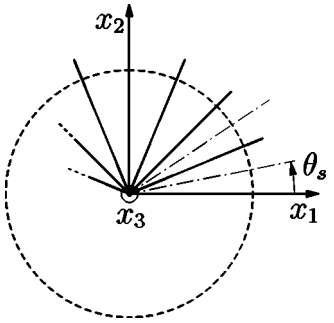

FIG. 23. Axisymmetric segmentation of particle field in (x_1,x_2) plane. The dashed circle indicates the initial suspension drop. The angle θ_s, $s=1,\ldots,N_s$ denotes the azimuthal location of the segments' center.

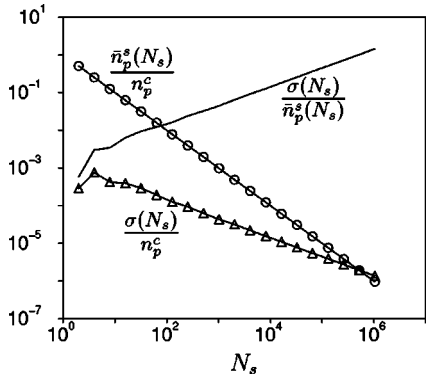

FIG. 24. Mean number of particles per segment $\bar{n}_p^s$ and standard deviation σ as a function of the number of segments N_s for initial suspension drop ($\bar{n}_p^s$ and σ are normalized by the total number of particles n_p^c). $\mathrm{Re}_d=100$, $N=64$, and $n_p^c=509\,645$.

to ensure that n_p^s is a measure of the local particle number density. Figure 24 shows the mean number of particles per segment $\bar{n}_p^s(N_s)$ and the corresponding standard deviation $\sigma(N_s)$ for a simulation with $n_p^c=509\,645$ ($\mathrm{Re}_d=100$, $\mathrm{St}=0.01$, $\mathrm{Fr}=44.7$, $\varrho_p/\varrho=1000$). In this case the suspension drop breaks up into six secondary blobs. Thus, criterion (i) requires the number of segments N_s to be much larger than the order of 10. Criterion (ii) requires the ratio $\sigma/\bar{n}_p^s$ to be much smaller than unity (Fig. 24). For the subsequent analysis $N_s=128$ was chosen.

The quantity $q(\theta_s,t)$ is decomposed into its Fourier coefficients according to

$$\hat{q}(k,t)=\frac{1}{N_s}\sum_{\theta_s} q(\theta_s,t)e^{-ik\theta_s}, \tag{18}$$

where $\hat{q}(k,t)$ is the Fourier coefficient associated with the azimuthal wavenumber $k=-N_s/2,\ldots,N_s/2-1$. Since $q(\theta_s,t)$ is a real quantity, the coefficients $\hat{q}(k,t)$ and $\hat{q}(-k,t)$ are complex conjugates. Therefore, the time evolution of the magnitude $|\hat{q}(k,t)|^2$ needs to be studied for positive k only.

Figure 25(a) shows the time evolution of the Fourier coefficients associated with the number of particles per segment $[q(\theta_s,t)=n_p^s(\theta_s,t)]$. From $t\approx 100$ on all Fourier coefficients start growing. For $100\lesssim t\lesssim 400$ the increase is approximately linear in the logarithmic-linear plot indicating an exponentially growing instability. The Fourier coefficient associated with wavenumber $k=6$ clearly predominates. This reflects a torus breakup into six (major) secondary blobs, as shown in Fig. 26(c). The second-strongest mode is associated with $k=8$ corresponding to the two additional (minor) secondary blobs in Fig. 26(c). It is worth noting that only at $t\approx 480$ the formation of bulges becomes visible when observing the settling torus [Fig. 26(b)]. The wavenumber selection, i.e., the onset of exponential growth with a certain mode predominating, occurs at a much earlier stage ($t\approx 150$), when it is clearly impossible to predict the number of secondary blobs by visual judgment only [Fig. 26(a)].

Figure 25(b) shows the time evolution of the Fourier coefficients associated with the mean particle settling velocity per segment $[q(\theta_s,t)=v_3^s(\theta,t)]$. The overall picture observed is the same as that in Fig. 25(a). The predominant

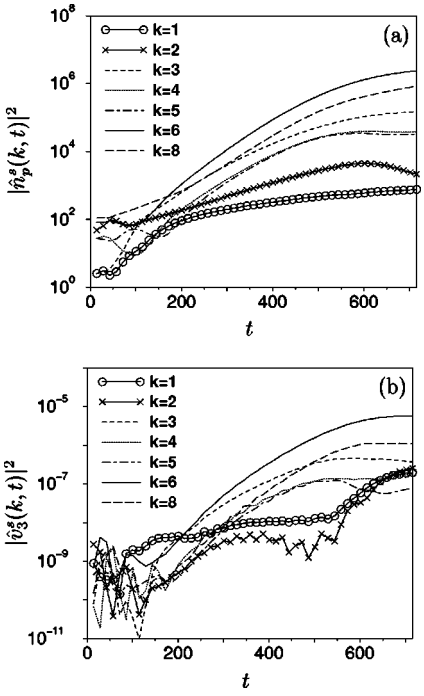

FIG. 25. Time evolution of the Fourier coefficients associated with (a) the number of particles per segment $n_p^s(\theta_s,t)$, and (b) the mean particle settling velocity $v_3^s(\theta_s,t)$. Same simulation as in Fig. 26.

mode is associated with wavenumber $k=6$, the second-strongest with $k=8$, however only for $t \gtrsim 500$. Also, the point in time when the wavenumber selection occurs cannot be identified as clearly as in Fig. 25(a).

Imposing artificial perturbations on the initial drop, as discussed in Sec. IV A, affects the time evolution of the Fourier coefficients. This is shown in Fig. 27. Here, the initial drop shape was perturbed according to Eq. (17) with $A_s = 0.01R$ and $l_s=4$. The shape perturbation causes the fourth mode, $k=4$, to grow rapidly shortly after the drop is released and then prevail during the entire settling process. The sixth mode $k=6$, which is due to the natural perturbations caused by the particle distribution, starts growing in the same way as

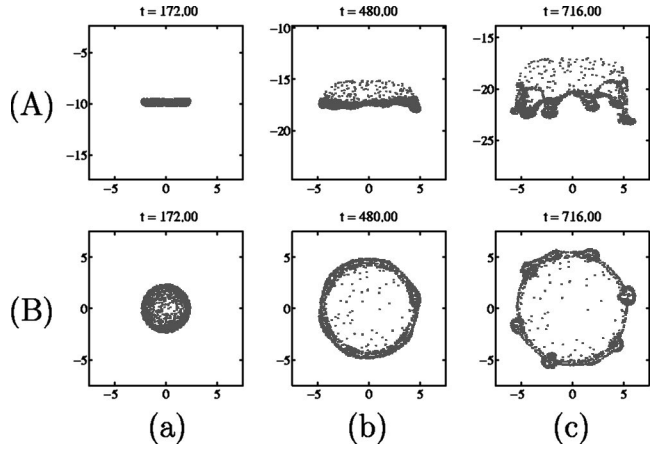

FIG. 26. Suspension drop at (a) $t=172$, (b) $t=480$, and (c) $t=716$. $\mathrm{Re}_d = 100$, $\mathrm{St}=0.01$, $\mathrm{Fr}=44.7$, $n_p^c = 509\,645$, $M=130$, and $N=64$. (A) Side view, (B) top view.

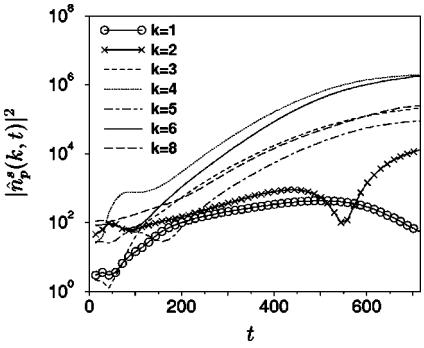

FIG. 27. Time evolution of the Fourier coefficients associated with the number of particles per segment for an initially perturbed suspension drop. Same parameters as in Fig. 26 and $A_s = 0.01R$, $l_s=4$.

in the unperturbed case (Fig. 25). As the instability develops, the sixth mode "catches up" with the fourth mode such that at $t=716$ the corresponding Fourier coefficients reach the same level. This results in a disintegrated drop with six secondary blobs as shown in Fig. 28. If the artificial perturbation level is increased ($A_s > 0.01R$) the predominance of the fourth mode is more pronounced yielding only four secondary blobs. If $A_s \ll 0.01R$ the fourth Fourier coefficient in Fig. 27 drops below the sixth mode and the disintegrated drop looks almost like the unperturbed one in Fig. 26.

V. SUMMARY AND CONCLUSIONS

The settling and breakup of suspension drops was investigated numerically using a pseudospectral method for the liquid phase and Lagrangian point-particle tracking for the particulate phase. The focus of the present investigation was on the physical processes affecting the instability and subsequent drop disintegration for moderate drop Reynolds numbers.

The case of low drop Reynolds numbers, $\mathrm{Re}_d \leqslant 0.1$, was used for validation purposes. Here, the suspension drop retains a roughly spherical shape while settling under gravity. A few particles leak away into a tail emanating from the rear of the drop. The theoretical streamline pattern provided by Nitsche and Batchelor[8] was very well reproduced in our simulations. Due to periodic boundaries in the pseudospectral method a hindered settling effect was observed: the drop settling velocity of a regular, three-dimensional array of suspension drops implied by our simulations may be considerably decreased compared with a single drop in infinite fluid.

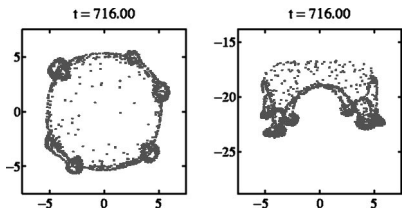

FIG. 28. Initially perturbed suspension drop. Top view (left), side view (right). Same parameters as in Fig. 26 and $A_s = 0.01R$, $l_s=4$.

The settling velocity in the limiting case of vanishing drop volume concentration was found to be in good agreement with the result by Nitsche and Batchelor.

In the case of moderate drop Reynolds numbers, $1 \leqslant \mathrm{Re}_d \leqslant 100$, the suspension drop deforms into a torus that eventually becomes unstable and breaks up into a number of secondary blobs. The particular way the torus breaks up is primarily determined by the drop Reynolds number and the distribution of the particles inside the drop and torus. With a fixed initial particle distribution an increasing Reynolds number leads to a larger number of secondary blobs. The deformation of the drop into a torus occurs at increasingly shorter times with increasing Reynolds number. The instability developing during the settling process was found to be very sensitive to the initial conditions, i.e., the initial distribution of particles, the initial drop shape, and the number of particles making up the suspension drop. In particular, the following observations were made: The random particle distribution was identified as the primary source of (natural) perturbations, which are crucial to the instability leading to torus breakup. Different initial particle positions affect the details of the disintegration process. They may even result in a different number of secondary blobs. If the number of real and/or computational particles is increased with otherwise fixed parameters, the particle distribution becomes more homogeneous. The natural perturbation level is decreased, which causes the settling torus to remain stable for a longer period of time and to break up into a larger number of secondary blobs. The crucial role of perturbations was further illustrated by initially perturbing the shape of the suspension drop. If the level of these artificial perturbations is large enough, a particular number of secondary blobs can be forced.

A grid resolution of $N \geqslant 64$ was sufficient to capture all relevant features of the disintegration process in the parameter range investigated. The periodic boundaries and the interpolation method used in the computation of the particle feedback force were shown to have a negligible influence.

To gain a deeper insight into the substructural effects leading to torus breakup, the particle field was analyzed from a spectral point of view. The time evolution of the Fourier coefficients in azimuthal direction of the torus associated with the local particle number density and the mean particle settling velocity was studied. The instability is characterized by exponentially growing modes associated with the wavenumbers in azimuthal direction. The fastest growing modes determine the number of secondary blobs obtained during breakup. The wavenumber selection, i.e., the onset of exponential growth with a certain mode predominating, was found to occur at an early stage during the torus formation long before the visible breakup sets in.

ACKNOWLEDGMENTS

Some of the results discussed in this paper were previously presented at the second International Conference on Computational Methods in Multiphase Flow (Bosse *et al.*[34]). The simulations were performed on the supercomputer NEC SX-5 at the Swiss Center of Supercomputing CSCS in Manno, Switzerland.

[1] C. T. Crowe, M. Sommerfeld, and Y. Tsuji, *Multiphase Flows with Droplets and Particles* (CRC, Boca Raton, 1998).
[2] J. F. Brady and G. Bossis, "Stokesian dynamics," Annu. Rev. Fluid Mech. **20**, 111 (1988).
[3] S. Chen and G. D. Doolen, "Lattice Boltzmann method for fluid flow," Annu. Rev. Fluid Mech. **30**, 329 (1998).
[4] M. W. Reeks, "On a kinetic equation for the transport of particles in turbulent flows," Phys. Fluids A **3**, 446 (1991).
[5] T. W. Pan, D. D. Joseph, and R. Glowinski, "Modelling Rayleigh-Taylor instability of a sedimenting suspension of several thousand circular particles in a direct numerical simulation," J. Fluid Mech. **434**, 23 (2001).
[6] R. Glowinski, "Finite element methods for incompressible viscous flow," in *Handbook of Numerical Analysis*, edited by P. G. Ciarlet and J. L. Lions (North-Holland, Amsterdam, 2003), Chaps. 8 and 9.
[7] R. Glowinski, T. W. Pan, T. I. Hesla, D. D. Joseph, and J. Periaux, "A fictitious domain approach to the direct numerical simulation of incompressible viscous flow past moving rigid bodies: Application to particulate flow," J. Comput. Phys. **169**, 363 (2001).
[8] J. M. Nitsche and G. K. Batchelor, "Break-up of a falling drop containing dispersed particles," J. Fluid Mech. **340**, 161 (1997).
[9] G. Machu, W. Meile, L. C. Nitsche, and U. Schaflinger, "Coalescence, torus formation and breakup of sedimenting drops: experiments and simulations," J. Fluid Mech. **447**, 299 (2001).
[10] M. Kojima, E. J. Hinch, and A. Acrivos, "The formation and expansion of a toroidal drop moving in a viscous fluid," Phys. Fluids **27**, 19 (1984).
[11] C. J. Koh and L. G. Leal, "The stability of drop shapes for translation at zero Reynolds number through quiescent fluid," Phys. Fluids A **1**, 1309 (1989).
[12] C. Pozrikidis, "The instability of a moving viscous drop," J. Fluid Mech. **210**, 1 (1990).
[13] N. Baumann, D. D. Joseph, P. Mohr, and Y. Renardy, "Vortex rings of one fluid in another in free fall," Phys. Fluids A **4**, 567 (1992).
[14] J. H. Walther and P. Koumoutsakos, "Three-dimensional vortex methods for particle-laden flows with two–way coupling," J. Comput. Phys. **167**, 39 (2001).
[15] M. R. Maxey and J. J. Riley, "Equation of motion for a small rigid sphere in a non-uniform flow," Phys. Fluids **26**, 883 (1983).
[16] M. R. Maxey, B. K. Patel, E. J. Chang, and L.-P. Wang, "Simulations of dispersed turbulent multiphase flow," Fluid Dyn. Res. **20**, 143 (1997).
[17] S. A. Orszag, "Numerical simulation of incompressible flows within simple boundaries: I. Galerkin (spectral) representations," Stud. Appl. Math. **50**, 293 (1971).
[18] U. Schumann, G. Grötzbach, and L. Kleiser, "Direct numerical simulation of turbulence," in *Prediction Methods for Turbulent Flows*, edited by W. Kollmann (Hemisphere, New York, 1980), p. 123.
[19] C. Canuto, M. Y. Hussaini, A. Quarteroni, and T. A. Zang, *Spectral Methods in Fluid Dynamics* (Springer, Berlin, 1988).
[20] M. R. Maxey and B. K. Patel, "Localized force representations for particles sedimenting in Stokes flow," Int. J. Multiphase Flow **27**, 1603 (2001).
[21] S. Elghobashi, "On predicting particle-laden turbulent flows," Appl. Sci. Res. **52**, 309 (1994).
[22] O. A. Druzhinin, "The influence of particle inertia on the two-way coupling and modification of isotropic turbulence by microparticles," Phys. Fluids **13**, 3738 (2001).
[23] A. S. Sangani and A. Acrivos, "Slow flow through a periodic array of spheres," Int. J. Multiphase Flow **8**, 343 (1982).
[24] A. A. Zick and G. M. Homsy, "Stokes flow through periodic arrays of spheres," J. Fluid Mech. **115**, 13 (1982).
[25] H. Hasimoto, "On the periodic fundamental solutions of the Stokes equations and their application to viscous flow past a cubic array of spheres," J. Fluid Mech. **5**, 317 (1959).
[26] A. S. Sangani, "Sedimentation in ordered emulsions of drops at low Reynolds numbers," ZAMP **38**, 542 (1987).
[27] G. Mo and A. S. Sangani, "A method for computing Stokes flow interactions among spherical objects and its application to suspensions of drops and porous media," Phys. Fluids **6**, 1637 (1994).
[28] D. D. Joseph and Y. Y. Renardy, *Fundamentals of Two-Fluid Dynamics* (Springer, Berlin, 1993), Vol. 2, Chapt. 9.
[29] S. Chandrasekhar, *Hydrodynamic and Hydromagnetic Stability* (Claren-

don, Oxford, 1961).
[30]P. K. Yeung and S. B. Pope, "An algorithm for tracking fluid particles in numerical simulations of homogeneous turbulence," J. Comput. Phys. **79**, 373 (1988).
[31]S. Balachandar and M. R. Maxey, "Methods for evaluating fluid velocities in spectral simulations of turbulence," J. Comput. Phys. **83**, 96 (1989).
[32]S. Sundaram and L. R. Collins, "A numerical study of the modulation of isotropic turbulence by suspended particles," J. Fluid Mech. **379**, 105 (1999).
[33]A. Kitagawa, Y. Murai, and F. Yamamoto, "Two-way coupling of Eulerian-Lagrangian model for dispersed multiphase flows using filtering functions," Int. J. Multiphase Flow **27**, 2129 (2001).
[34]T. Bosse, C. Härtel, E. Meiburg, and L. Kleiser, "Simulation of settling and break-up of suspension drops in a fluid," in *Computational Methods in Multiphase Flows II, Advances in Fluid Mechanics*, edited by A. A. Mammoli and C. A. Brebbia (WIT, Southampton, 2003), p. 149.